A Model and Numerical Framework for the Simulation of Solid-Solid Phase Transformations

Garrett J. Hall[a] and Sanjay Govindjee[a]

[a]Structural Engineering, Mechanics, and Materials
Department of Civil and Environmental Engineering
University of California, Berkeley
Berkeley, CA 94720-1710

ABSTRACT

A model and its computational realization for the simulation of solid-solid phase transformations of the type observed in shape memory alloys is presented. The model includes both mechanically and thermally driven phase changes. It is based on mixture theory combined with a suitable kinetic model for phase evolution and explicitly accounts for reorientation of the crystalline anisotropy and the associated symmetry changes which are essential to the observance of memory effects. Computational methods employing the energetic potentials, which are required in order to estimate the transformation history, are discussed in detail. Numerical examples are provided which illustrate the behavior of the model for sample cubic $\leftrightarrow$ tetragonal and cubic $\leftrightarrow$ orthorhombic shape memory materials. The complex behavior predicted is similar to that seen in selected physical experiments and is indicative of the power of the proposed modelling methodology. In particular the model predicts unsymmetric response in tension and compression, loss of shape memory effect in polycrystalline settings with high symmetry martensites, and qualitative twin structures among many other complex behaviors.

Keywords: Shape Memory Alloys, Phase Transformation

Further author information:
S.G.: E-mail: govindjee@ce.berkeley.edu
G.J.H.: E-mail: gjhall@ce.berkeley.edu

1. INTRODUCTION

The rapidly expanding body of literature addressing topics related to shape memory alloys is a testament to the complexity of the phenomena as well as the growing interest in applying it advantageously in industrial/commercial applications. With this interest comes a need for computational models which can be used to estimate the behavior of such materials in real world problems with general boundary conditions. Although a large number of detailed descriptions of the shape memory process have been advanced, the need for computational simulations distinguishes between the theoretical and numerical models, both of which are valuable in their own right. This paper is concerned with a three dimensional model which attempts to strike a balance between the desire to include a reasonably detailed description of the physical process with the need to solve complex boundary value problems numerically. The work is a direct extension of the one dimensional model proposed in Govindjee & Hall (1999a).

The general difficulty in modeling the shape memory effect and related solid-solid phase transformations is elucidated nicely in the body of literature that aims to treat the problem from a strictly elastic equilibrium viewpoint; see for example Ball & James (1987, 1992), Milke, Kuczma & Theil (1998), Smyshlyaev & Willis (1999), and further references therein. The central point is that the problem is governed by a non-convex structure and that the equilibrium energy admits a collection of (point group) symmetry related minimizers. Further, the infimum of the elastic energy is not attained by the energy functional and this naturally leads to the production of fine microstructure. From a numerical perspective this model structure leads directly to a problem that will display strong computational grid dependence and a lack of global convergence. To circumvent these issues, the notion of a relaxed problem has been introduced (see for example Kohn 1991) by means of a quasi-convex energy functional; the primary property of this relaxed problem is that it posses the same infimum of the original problem and furthermore it attains the infimum. Utilizing this notion Carstensen & Plecháč (1997, 1998) have shown how one may numerically solve general boundary value problems, essentially using standard methods for elasticity, and further extract microstructural information from the solutions – viz. the Young measure of the strain field which in this context is basically the volume fraction of the phases. They were able to do this for the special case of a two-well energy functional. The extension to a more practical number of wells, say 13 for example in the case of Nickel-Titanium alloys, is complicated by the construction of the relaxed energy functional; see for example Smyshlyaev & Willis (1999) for a discussion of the three-well problem.

The complexity of the pure elastic viewpoint has led to the development of a parallel body of literature that deals with a variety of regularized versions of the above described problem. Popular in this regard are theories that utilize some type of homogenization theory in conjunction with a set of internal variables that characterized the microstructure of the material and its evolution; see for example Boyd and Lagoudas (1996a, 1996b), Huang & Brinson (1998), and further references therein. Central to using such models in a numerical setting is the construction of evolution equations for the internal variables that characterize the microstructure of the material. These are often postulated as in Lubliner & Auricchio (1996) or developed based upon specific microstructural geometry assumptions as in Huang & Brinson (1998). Here we follow along the lines proposed by Abeyaratne, Kim & Knowles (1994) and Achenbach & Müller (1985). In this line of reasoning the evolution equations are developed using transition state kinetics which are based on methods typically employed in statistical physics/kinetics.

The basis of the model is encapsulated in the idea that the martensitic variants may be considered a family of idealized thermoelastic materials coexisting in a mixture which is parameterized by a set of volume fractions. To this is added the simplifying assumption of a pointwise homogeneous mixture as motivated by the diffusionless nature of experimentally observed martensitic transformations. The evolution of the system is then assumed to be governed by a simple kinetic law based on statistical physics and the explicit computation of the energetics of the problem. This approach has the advantages of being independent of spatial dimension while capturing the symmetry changes induced by both crystalline reorientation and phase change. From a computational viewpoint it is particularly noteworthy that the model is robust in a numerical setting. These points are highlighted in the presented work as outlined below.

Section 2 briefly describes the physics of shape memory in order to motivate the kinematics of the model presented in Section 3. Then after discussing the mass balance, energy structure, and kinetics of the model, the treatment of the required barrier height calculations is detailed. This leads into Section 4 where the numerical issues of a discrete implementation are covered, and Section 5 which provides a number of numerical simulations covering two classes of shape memory materials.

2. DEFORMATION, TWINNING, AND KINEMATICS

The development of the constitution begins with the assumed existence of a family of idealized materials comprising a bounded deformable continuum moving in $\mathbb{R}^3$. The motion may be characterized in terms of a reference and a spatial configuration which are denoted by Ω_o and Ω respectively. In considering the composition of the continuum, we will **for the moment** adopt the notion that any point in the continuum is occupied by a single material $\alpha \in \{1, 2, 3, \dots v+1\}$. This approach naturally leads to the existence of interfacial surfaces dividing volumes occupied by different materials.
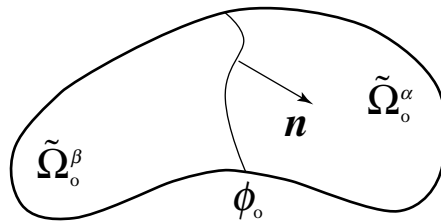

Figure 1. Configuration of an interfacial surface ϕ_o with normal $\boldsymbol{n}$ dividing the reference configuration of a body Ω_o.

As an example, the illustration of Figure 1 shows compatible subregions of the (reference) body divided into portions $\tilde{\Omega}_o^\alpha$ and $\tilde{\Omega}_o^\beta$ by the phase boundary ϕ_o. These regions map into the spatial configurations $\tilde{\Omega}^\alpha$, $\tilde{\Omega}^\beta$ and the spatial phase boundary ϕ. The physics of the problem require that

the deformation map be continuous in the manner

$$\llbracket \boldsymbol{x} \rrbracket = \boldsymbol{x}^\alpha - \boldsymbol{x}^\beta = \boldsymbol{0}, \tag{1}$$

where $\llbracket \cdot \rrbracket$ denotes the value of the jump across the phase boundary. Superscripts α and β denote maps associated with regions $\widetilde{\Omega}_o^\alpha$ and $\widetilde{\Omega}_o^\beta$ respectively. Defining the deformation gradient $\boldsymbol{F}$ in the usual manner, the well known jump condition

$$\llbracket \boldsymbol{F} \rrbracket = \boldsymbol{f} \otimes \boldsymbol{n} \tag{2}$$

may be derived as a geometric condition of compatibility where $\boldsymbol{f}$ is a vector in the spatial configuration, and $\boldsymbol{n}$ is the normal to the surface ϕ in the reference configuration; see Truesdell & Toupin (1960) and Truesdell & Noll (1965) for a formal discussion of surfaces of discontinuity. Expressed in terms of the Right Cauchy Green deformation tensor ($\boldsymbol{C} = \boldsymbol{F}^T \boldsymbol{F}$) the jump condition has the equivalent forms

$$\begin{aligned} \llbracket \boldsymbol{C} \rrbracket &= \boldsymbol{f}^\alpha \otimes \boldsymbol{n} + \boldsymbol{n} \otimes \boldsymbol{f}^\alpha - \gamma^2 \boldsymbol{n} \otimes \boldsymbol{n} \\ &= \boldsymbol{f}^\beta \otimes \boldsymbol{n} + \boldsymbol{n} \otimes \boldsymbol{f}^\beta + \gamma^2 \boldsymbol{n} \otimes \boldsymbol{n}, \end{aligned} \tag{3}$$

where $\boldsymbol{f}^\alpha = (\boldsymbol{F}^\alpha)^T \boldsymbol{f}$, $\boldsymbol{f}^\beta = (\boldsymbol{F}^\beta)^T \boldsymbol{f}$, and $\gamma^2 = \boldsymbol{f} \cdot \boldsymbol{f}$. It is also interesting to note from Eq.(2) the geometric relation

$$\boldsymbol{f}^\alpha - \boldsymbol{f}^\beta = \gamma^2 \boldsymbol{n}. \tag{4}$$

Next, applying the jump condition to the Green Lagrange strain measure $\boldsymbol{E} = \frac{1}{2}(\boldsymbol{C} - \boldsymbol{1})$ results in the relation

$$\llbracket \boldsymbol{E} \rrbracket = \tfrac{1}{2} \llbracket \boldsymbol{C} \rrbracket, \tag{5}$$

which is often given in the infinitesimal form

$$\llbracket \boldsymbol{\varepsilon} \rrbracket = \tfrac{1}{2}(\widetilde{\boldsymbol{f}} \otimes \boldsymbol{n} + \boldsymbol{n} \otimes \widetilde{\boldsymbol{f}}), \tag{6}$$

where $\tilde{\boldsymbol{f}}$ is the leading order approximation to either $\boldsymbol{f}^\alpha$ or $\boldsymbol{f}^\beta$. The above results, which arise from arguments regarding the behavior of the deformation map across the surface of discontinuity, may be further specialized to a class of piecewise homogeneous motions which are of the form

$$\boldsymbol{F}^\alpha = \boldsymbol{Q} \boldsymbol{F}^\beta \boldsymbol{H}, \tag{7}$$

where for the moment it is sufficient to consider $\boldsymbol{Q}$ and $\boldsymbol{H}$ to be elements of the proper orthogonal group[†] over $\mathbb{R}^3$. This implies that $\det(\boldsymbol{F}^\alpha) = \det(\boldsymbol{F}^\beta)$, and by defining $\boldsymbol{a} = (\boldsymbol{F}^\beta)^{-1} \boldsymbol{f} = (\boldsymbol{C}^\beta)^{-1} \boldsymbol{f}^\beta$ the relation

$$\boldsymbol{a} \cdot \boldsymbol{n} = 0 \tag{8}$$

follows from the determinate condition. The definition of $\boldsymbol{a}$ also allows one to express the jump condition of Eq.(2) in the well known form

$$\boldsymbol{F}^\alpha = \boldsymbol{F}^\beta(\boldsymbol{1} + \boldsymbol{a} \otimes \boldsymbol{n}) \tag{9}$$

[†]Gurtin (1983) provides proof of Ericksen's theorem regarding the nature of both $\boldsymbol{Q}$ and $\boldsymbol{H}$ as π rotations for twinning deformations.

where the operator $\mathbf{1}+\boldsymbol{a}\otimes\boldsymbol{n}$ is noted to exist in the reference configuration. An equivalent derivation which is often given in the literature formulates the spatial operator $\mathbf{1}+\boldsymbol{f}\otimes\boldsymbol{m}$ so that

$$\boldsymbol{F}^\alpha = (\mathbf{1}+\boldsymbol{f}\otimes\boldsymbol{m})\boldsymbol{F}^\beta \tag{10}$$

where $\boldsymbol{m}=(\boldsymbol{F}^\beta)^{-1}\boldsymbol{n}$. By the same arguments as used previously, it is also found that $\boldsymbol{f}\cdot\boldsymbol{m}=0$ so that both the operators $\mathbf{1}+\boldsymbol{a}\otimes\boldsymbol{n}$ and $\mathbf{1}+\boldsymbol{f}\otimes\boldsymbol{m}$ have the characteristic equation $(\lambda-1)^3=0$, and may be interpreted as a simple shear. From a crystallographic viewpoint, the existence of regions (twins) which approximate the particular kinematic relationships derived above are essential to the observance of shape memory as discussed next.

A conceptual understanding of the shape memory phenomena exhibited by certain alloys can be attained through the consideration of a material which may exist in two solid phases belonging to different crystal systems. Based on the measurable lattice parameters of the two systems, a homogeneous deformation process from the high symmetry phase to the lower symmetry phase may be described by a right stretch deformation tensor $\boldsymbol{U}$ which minimizes the strain energy of the solid. However, if the point group of the high symmetry phase (termed austenite) is given by $\mathcal{P}$, then it is clear that all unique variations of

$$\widehat{\boldsymbol{U}} = \boldsymbol{H}\boldsymbol{U}\boldsymbol{H}^T \quad , \quad \boldsymbol{H}\in\mathcal{P} \tag{11}$$

are admissible minimizers as well. The resulting set $\{\boldsymbol{U}^1,\boldsymbol{U}^2\ldots\boldsymbol{U}^v\}$ describes the "lattice correspondence" variants of the low symmetry phase, which we will hereafter refer to as martensitic variants. The term twin compatible variants is defined by the satisfaction of Eq.'s(9, 10, or 6) with regard to the deformation $\boldsymbol{U}$. For example, satisfaction of the expression

$$[\![\boldsymbol{\varepsilon}]\!] = \widehat{\boldsymbol{\varepsilon}}(\boldsymbol{U}^\alpha) - \widehat{\boldsymbol{\varepsilon}}(\boldsymbol{U}^\beta) = \tfrac{1}{2}(\widetilde{\boldsymbol{f}}\otimes\boldsymbol{n}+\boldsymbol{n}\otimes\widetilde{\boldsymbol{f}}) \tag{12}$$

implies that the variants defined by $\boldsymbol{U}^\alpha$ and $\boldsymbol{U}^\beta$ are (first order) twin compatible. The structure of Eq.(12) also provides the sufficient (though not necessary) condition that the variants α and β are not twin compatible when $[\![\boldsymbol{\varepsilon}]\!]$ has full rank. This can be proven by considering the characteristic equation

$$f(\lambda) = -\lambda^3 + \mathrm{I}([\![\boldsymbol{\varepsilon}]\!])\lambda^2 - \mathrm{II}([\![\boldsymbol{\varepsilon}]\!])\lambda + \mathrm{III}([\![\boldsymbol{\varepsilon}]\!]) \tag{13}$$

and the fact that $\mathrm{III}([\![\boldsymbol{\varepsilon}]\!]) = \det(\widetilde{\boldsymbol{f}}\otimes\boldsymbol{n}+\boldsymbol{n}\otimes\widetilde{\boldsymbol{f}}) = 0$. This condition can be used to easily determine variants which are not possibly twin related. The existence of such twin compatible variants, and the ability of the material to transform between them without inducing permanent slip deformation, is the key to the observance of shape memory.

A description of the process is as follows: Taking the reference state as a single crystal of the high symmetry phase, the unstressed material is sufficiently cooled so that a solid-solid phase transformation occurs resulting in a self-accommodating fine mixture of the low symmetry martensite phases. Depending upon the symmetry of the phases, subsequent mechanical loading may produce a significant rearrangement of the martensitic structure to accommodate the load (resulting in an apparently permanent offset to the viewer at a macroscopic level). However, upon reheating the shape change induced by this deformation process is recoverable through a return to the high symmetry phase. The magnitude of the shape memory, i.e. the set of fully recoverable strains, is a function of the symmetry change between the phases. For materials in which all of the variants are

twin-related in the sense described previously, the recoverable strains are the convex set bounded by the lattice correspondent (Bain) strains. An example is provided by the cubic to tetragonal solid-solid phase transformation for which there are three variants and the infinitesimal recoverable strain set $\mathcal{L}$ is given by (Bhattacharya & Shu 1998)

$$\mathcal{L} = \left\{ \boldsymbol{\varepsilon} \;\middle|\; \boldsymbol{\varepsilon} = \sum_{i=1}^{3} \kappa_i \boldsymbol{\varepsilon}^i \quad, \quad \sum_{i=1}^{3} \kappa_i = 1 \quad, \quad \kappa_i \geq 0 \right\}. \tag{14}$$

It is worth noting that in the general case not all transformations have this feature; e.g. not all of the cubic to monoclinic variants are twin compatible, just as the austenitic phase is in general not a twin for a variant of the martensitic phase. This observation is related to the fine twinning structures and formation of plate variants that are seen experimentally. For the present purpose, we take the recoverable strain set $\mathcal{L}$ as an essential feature for inclusion in the constitutive model; for further discussion of twin compatibility in various alloys see Bhattacharya & Shu (1998), Bhattacharya (1993), Bhattacharya & Kohn (1996) and references therein.

3. CONSTITUTIVE MODEL

From a modeling perspective the embedding of accurate physics, or in this case detailed crystallography, is often at odds with the need to construct a constitution which results in a tractable boundary value problem. In particular, the development of a model which requires the tracking of interfacial boundaries over a large three dimensional structural system is currently not feasible within the confines of the need for moderate computational expense. At the other extreme, the complexity of solid-solid phase transformations implies that purely phenomenological models cannot simulate with any confidence trends beyond those used in their calibration. The work presented here is an attempt to reconcile these problems through the application of classical mixture theory to a family of $v + 1$ idealized thermoelastic materials representing the austenite phase and the v variants of the martensitic phase. This approach, which does not endeavor to rigorously reproduce the richness of crystalline structure that can exist in solid transforming materials, has the advantage of capturing the recoverable strain set $\mathcal{L}$ as well as the essential physics of the transformation.

The classical development of mixture theory (Atkin & Craine 1976) allows for each point of a body (Ω) to be simultaneously occupied by any number of constituent materials which are free to enjoy their own path in the field variables (e.g. space, temperature). By taking the history of the composite body as a functional of the constituent histories, a wide range of complex phenomena (e.g. diffusion, chemical reactions, etc.) can be modeled. However, in light of the diffusionless nature of the phase transitions under consideration, it is reasonable to begin with the assumption of a pointwise homogeneous mixture. That is, rather than considering the individual motions $\boldsymbol{x} = \boldsymbol{\varphi}^\alpha(\boldsymbol{X}^\alpha, t)$, to each point $\boldsymbol{X} \in \Omega_o$ is assigned a single spatial position $\boldsymbol{x}$, a single absolute temperature θ, and a set of fractions ξ^α representing the volume fraction of each material at that point. The time history is then taken as the sufficiently smooth functions

$$\boldsymbol{x} = \boldsymbol{\varphi}(\boldsymbol{X}, t) \quad, \quad \theta = \hat{\theta}(\boldsymbol{X}, t) \quad, \quad \xi^\alpha = \hat{\xi}^\alpha(\boldsymbol{X}, t) \tag{15}$$

from which the deformation gradient $\boldsymbol{F}$ and the Green-Lagrange strain tensor $\boldsymbol{E} = \frac{1}{2}(\boldsymbol{F}^T \boldsymbol{F} - \boldsymbol{1})$ are defined. Although a number of conceptual interpretations may be applied to Eq.(15) with regard

6

to the problem at hand, for the moment it is sufficient to consider the model as a superposition of idealized crystalline lattices whose skeletal motion is approximated by the macroscopic deformation. While beyond the scope of the present work, the general applicability of this concept to various problems is discussed at length by Zanzotto (1996). We next investigate relations predicated by the mass conservation principal.

Conservation of Mass

In the present work it is presumed that the ratio (V^α/V) of volume occupied by material α to the total volume takes on a finite value ξ^α in the limit of vanishing volume V. For a fixed set of materials this implies that the volume fractions satisfy

$$\sum_\alpha \xi^\alpha = 1 \quad ; \quad 0 \le \xi^\alpha \le 1 \tag{16}$$

at the resulting point. By then assigning to each member of the mixture a reference density ρ_o^α which maps to a unique density ρ^α in the spatial configuration, the mass m of the body may be computed as

$$m = \int_\Omega \sum_\alpha \rho^\alpha \xi^\alpha, \tag{17}$$

where Ω denotes integration over the spatial configuration of the body. Neglecting the possibility of mass flux across the bounding surface $\partial\Omega$, mass conservation states that the time rate of change of the mass is zero; i.e.,

$$\dot{m} = \frac{d}{dt} \int_\Omega \sum_\alpha \rho^\alpha \xi^\alpha = 0. \tag{18}$$

With the kinematic assumption that a single velocity vector $\boldsymbol{v} = \hat{\boldsymbol{v}}\left(\boldsymbol{x}, t\right)$ describes the motion at each point, the transport theorem takes on the form

$$\dot{m} = \int_\Omega \sum_\alpha \left[\overline{\dot{\rho^\alpha \xi^\alpha}} + \rho^\alpha \xi^\alpha \mathrm{div}(\boldsymbol{v}) \right] = 0 \tag{19}$$

for the solid mixture. Then, by defining the Jacobian of the deformation gradient $J = \det(\boldsymbol{F})$ the fundamental relations $\rho_o^\alpha = \rho^\alpha J$ and $\frac{d}{dt} J = \mathrm{div}(\boldsymbol{v}) J$ are also found to maintain applicability in the present setting. Taking account of this with regard to Eq.(19) results in the equivalent statement of mass conservation

$$\dot{m} = \int_\Omega \sum_\alpha \rho^\alpha \dot{\xi}^\alpha = 0. \tag{20}$$

Through the limitation imposed by assuming that the reference densities of all the materials are negligibly close, $(\rho_o^\alpha = \rho_o^\beta \quad \forall\, \alpha, \beta)$, the conclusion that each point in the body satisfies $\sum_\alpha \rho^\alpha \dot{\xi}^\alpha = 0$ may be modified to state

$$\sum_\alpha \dot{\xi}^\alpha = 0. \tag{21}$$

In accordance with this simplification we will no longer place superscripts on the densities; it will be understood that they are all taken as equal. As will be seen, the fundamental restrictions of Eq.'s (16) and (21) are directly related to the structure of the phase transformation equations. However, in order to discuss the transformation kinetics, the constituent and mixture energy functions must be introduced first.

Potential Energy Functions

Viewing the mixture as a collection of idealized thermoelastic materials, a simple energy function $\psi^\alpha = \widehat{\psi^\alpha}(\boldsymbol{E}, \theta)$ may be constructed for each constituent such that $\rho_o \psi^\alpha$ gives the Helmholtz free energy per unit volume. Motivated by the kinematic considerations outlined in Section 2, a free energy function is assigned to the austenite phase as well as one for each of the v martensitic variants. The free energy of the mixture is then comprised of, but not limited to, the sum of the individual free energy functions multiplied by their respective volume fractions. Additionally, an energy term $\epsilon = \widehat{\epsilon}(\boldsymbol{E}, \theta, \xi^\alpha)$ arising from material interaction, e.g. an interfacial energy term, may be included in the approximation of the mixture free energy

$$\rho_o \Psi = \sum_\alpha \xi^\alpha \rho_o \psi^\alpha + \epsilon, \tag{22}$$

where it is clear that $\Psi = \widehat{\Psi}(\boldsymbol{E}, \theta, \xi^\alpha)$. The particular free energy functions chosen are an extension of those used in the one dimensional implementation presented in Govindjee & Hall (1999a) based upon Abeyaratne, Kim & Knowles (1994). For material α, the mechanical and thermomechanical terms of the free energy are given by

$$\chi^\alpha = \tfrac{1}{2}(\boldsymbol{E} - \boldsymbol{E}^{\alpha_t}) : \mathbb{C}^\alpha : (\boldsymbol{E} - \boldsymbol{E}^{\alpha_t}) - (\Delta\theta)\boldsymbol{E}^{\alpha_\theta} : \mathbb{C}^\alpha : (\boldsymbol{E} - \boldsymbol{E}^{\alpha_t}) \tag{23}$$

where $\boldsymbol{E}^{\alpha_t}$ is the Bain strain, $\mathbb{C}^\alpha$ is the fourth order elasticity tensor, $\boldsymbol{E}^{\alpha_\theta}$ is the thermal expansion tensor, and $\Delta\theta = \theta - \theta_o$ is the temperature change relative to the reference state. Out of convenience, the materials are ordered such that austenite corresponds with $\alpha = 1$ in which case $\boldsymbol{E}^{\alpha_t=1_t} = \boldsymbol{0}$. It is also noted that in general $\mathbb{C}^\alpha$ and $\boldsymbol{E}^{\alpha_\theta}$ are anisotropic in accordance with the crystal system of material α. In addition to $\hat{\chi}^\alpha(\boldsymbol{E}, \theta)$, the free energy also has a purely thermal contribution $\hat{\phi}^\alpha(\theta)$ in the form

$$\phi^\alpha = \rho_o c \theta (1 - \log(\theta/\theta_o)) - \rho_o \lambda^\alpha (1 - \theta/\theta_o), \tag{24}$$

where the heat capacity c is assumed constant for all materials. Similarly the latent heat λ^α is taken as equal for all the martensitic variants, and zero for austenite ($\lambda^{\alpha=1} = 0$). Finally, in the interest of simplicity, the specification of ϵ is deferred; for the moment it is assumed that $\epsilon \approx 0$. The resulting free energy

$$\rho_o \Psi = \sum_\alpha \xi^\alpha \rho_o \psi^\alpha = \sum_\alpha \xi^\alpha (\chi^\alpha + \phi^\alpha) \tag{25}$$

is the Helmholtz free energy per unit volume for the mixture. As a consequence of this choice, the effective second Piola-Kirchhoff stress $\boldsymbol{S}$ is determined as the derivative of the Helmholtz Potential with respect to the Green-Lagrange strain

$$\boldsymbol{S} \;=\; \rho_o \frac{\partial \Psi}{\partial \boldsymbol{E}} \;=\; \sum_\alpha \frac{\partial \chi^\alpha}{\partial \boldsymbol{E}} \tag{26}$$

$$\boldsymbol{S} \;=\; \sum_\alpha \xi^\alpha \mathbb{C}^\alpha : [\boldsymbol{E} - \boldsymbol{E}^{\alpha_t} - (\Delta\theta)\boldsymbol{E}^{\alpha_\theta}], \tag{27}$$

where the result has been expressed as a sum of contributions from each material. Similarly, the second derivative $\rho_o \frac{\partial^2 \Psi}{\partial(\boldsymbol{E})^2}$ defines an effective modulus for the mixture denoted by

$$\mathbb{C} = \sum_\alpha \xi^\alpha \mathbb{C}^\alpha, \tag{28}$$

8

where the composite elasticity tensor is a sum of contributions from the constituent materials. Typically the austenite ($\alpha = 1$) phase of materials exhibiting memory has a cubic structure, whereas the variants of the martensitic phase are particular orientations of a lower symmetry crystalline structure. Through changes in the volume fractions, it is seen that Eq.(28) reflects the changing anisotropy of the material. The specification of the evolution equations governing the volume fractions is aided by the construction of a Gibbs like function.

Starting with the free energy function of Eq.(25), the transformation

$$G = \inf_E \left\{ \rho_o \Psi - \boldsymbol{S} : \boldsymbol{E} \right\} \tag{29}$$

defines $G = \widehat{G}(\boldsymbol{S}, \theta, \boldsymbol{\xi})$ where as before $\boldsymbol{S}$ is the second Piola-Kirchhoff stress measure for the mixture, θ is the absolute temperature, and $\boldsymbol{\xi}$ represents the volume fractions arranged as a vector. By defining $\hat{g}^\alpha(\boldsymbol{S}, \theta, \boldsymbol{E})$ as the potential energy function $g^\alpha = \rho_o \psi^\alpha - \boldsymbol{S} : \boldsymbol{E}$, Eq.(29) may be rewritten as

$$G = \inf_E \left\{ \rho_o \Psi - \boldsymbol{S} : \boldsymbol{E} \right\} = \inf_E \left\{ \sum_\alpha \xi^\alpha g^\alpha \right\}. \tag{30}$$

In this form it is seen that when the mixture is composed of a single material, say $\xi^\beta = 1$, the Gibbs energy is determined by the critical point of the function g^β. Under an applied stress field differences in the single variant Gibbs energies at varying volume fractions are taken as indicators of the driving potential for transformation. A framework for modeling phase transformation/reorientation is considered next.

Transformation Kinetics

The transformation kinetics follow from the work of Abeyaratne, Kim & Knowles (1994), Abeyaratne & Kim (1997), and the body of work by Müller and co-workers (e.g. Achenbach 1989); see also Govindjee & Hall (1999a). The framework is based on statistical physics; the essential postulate being that the net probability of transformation can be estimated from the energetic barriers between the individual phases. This idea is captured in the equation set

$$\dot{\xi}^\alpha = \sum_\beta^{\beta \neq \alpha} \omega \left(P_{\beta\alpha} \xi^\beta - P_{\alpha\beta} \xi^\alpha \right), \tag{31}$$

where $\dot{\xi}^\alpha$ is the transformation rate for material α. The terms $P_{\beta\alpha}$ and $P_{\alpha\beta}$ estimate the transition probability from material β to α and α to β respectively. By attenuating these probabilities by the corresponding volume fraction from which the transformation is occurring, the difference between the resulting products multiplied by the attempt frequency ω approximates the transformation rate. This rate dependent model may be expressed compactly as:

$$\dot{\boldsymbol{\xi}} = \boldsymbol{Q}\boldsymbol{\xi}, \tag{32}$$

where $\boldsymbol{\xi}$ is the vector of volume fractions and $\boldsymbol{Q}$ is the matrix assembly of terms from Eq.(31). Since $\boldsymbol{Q}$ is the generator of the evolution process in the volume fractions, it is worth noting that any column sum from $\boldsymbol{Q}$ is equal to zero thereby satisfying the conservation of mass statement given by Eq.(21).

9

Denoting k as Boltzmann's constant and Δv as the transforming volume, an Eyring model is used to calculate the admissible transition probabilities $P_{\alpha\beta}$ as

$$P_{\alpha\beta} = \exp\left[\frac{-\Delta v b_{\alpha\beta}}{k\theta}\right] \tag{33}$$

in which $b_{\alpha\beta}$ represents the energetic barrier in the transition from α to β. As alluded to previously, the barrier energy arises from the potential energy profile as parameterized by the volume fractions. In particular the barrier for transition from material α to material β is taken as the difference between the energy of constituent α and the critical point on the energy path between the two materials. This is represented by

$$b_{\alpha\beta} = \hat{b}_{\alpha\beta}\left(\boldsymbol{S}, \theta\right) = G_{\alpha\beta} - G\left(\boldsymbol{S}, \theta, \xi^{\alpha} = 1\right) \geq 0 \tag{34}$$

where for a fixed value of stress, $G_{\alpha\beta}$ may be thought of as the minimum point over the set of strains where the potential functions g^{α} and g^{β} are equal in value. A more precise definition is given in the following section in which the computational aspects of Eq.(34) are discussed.

Barrier Energy Calculations

Previous implementations of this model have been unidimensional at the constitutive level; the current implementation includes modifications to extend it to three spatial dimensions. To simplify matters in the present investigation we limit our focus to those materials which have twin compatible variants, and therefore recoverable strain sets of the form given by Eq.(14). As an example, consider a material with a cubic austenite phase and an orthorhombic martensitic phase. This case produces six martensitic variants, all of which are twin compatible as per the definition of Eq.(6) (Bhattacharya & Kohn 1996). Accounting for austenite, there are then a total of 21 unique $b_{\alpha\beta}$ computations which are necessary to determine $\boldsymbol{Q}$. Also, contrary to the situation in one dimension (Govindjee & Hall 1999a), calculation of the barrier energy under three dimensional stress states does not permit a closed form solution. For these reasons, in this section we discuss an approach for computing the barrier heights in a reasonably efficient fashion.

If the constitution is unidimensional, the term $G_{\alpha\beta}$ is interpreted as the intersection between the potential functions g^{α} and g^{β}; a point. However, in higher dimensions the intersection is no longer a point, and a different approach is necessary. The desire is to find the path of minimum energy subject to the restriction that the values of g^{α} and g^{β} are equal. To this end, $G_{\alpha\beta}$ may be precisely defined as the value of the Lagrangian potential

$$\Pi = \widetilde{\Pi}\left(\lambda, \boldsymbol{E}\right) = g^{\beta} + \lambda\left(g^{\alpha} - g^{\beta}\right) \tag{35}$$

at its critical point (note that $\boldsymbol{S}$ and θ are fixed in Π). In words, it is desired to minimize the energy g^{β} within the space defined by $g^{\beta} = g^{\alpha}$. In this context the Lagrange multiplier λ plays the role of a volume fraction as can be seen by considering the critical equations arising from this formulation:

$$\frac{\partial\Pi}{\partial\boldsymbol{E}} = \lambda\frac{\partial g^{\alpha}}{\partial\boldsymbol{E}} + (1 - \lambda)\frac{\partial g^{\beta}}{\partial\boldsymbol{E}} = 0 \tag{36}$$

$$\frac{\partial\Pi}{\partial\lambda} = g^{\alpha} - g^{\beta} = 0. \tag{37}$$

In one dimension, both equations and all the arguments were scalar and this trivialized the problem to allow for the direct solution for the barrier energy. In three dimensions an identical strategy proves intractable, so it is necessary to consider an alternate approach whereby Eq.(36) is first solved as a function of λ, i.e., $\boldsymbol{E}^\pi = \widetilde{\boldsymbol{E}}^\pi(\lambda)$. With this result, Eq.(37) may be solved as a scalar equation of a scalar variable (λ). Furthermore, this point represents the extremum of the potential $\widetilde{G}\left(\boldsymbol{S}, \theta, \xi^\gamma = 0 \ \forall \gamma \neq \alpha, \beta\right)$. A summary of the approach is given by Algorithm 1 below.

ALGORITHM 1. Barrier Energy Computation

1. *Input :*

$$\{\boldsymbol{S} \ , \ \theta \ , \ \alpha \ , \ \beta\} \tag{38}$$

2. *Formulate Π:*

$$\Pi \ = \ \lambda g^\alpha + (1-\lambda)g^\beta \tag{39}$$

3. *Find critical point w.r.t $\boldsymbol{E}$:*

$$\boldsymbol{E}^\pi = \left\{\boldsymbol{\tau} \ \middle| \ \frac{\partial \widetilde{\Pi}(\lambda, \boldsymbol{\tau})}{\partial \boldsymbol{\tau}} = 0\right\} \tag{40}$$

4. *Find critical point w.r.t λ:*

$$\lambda^\pi = \left\{\eta \ \middle| \ \frac{d\widetilde{\Pi}\left(\eta, \widetilde{\boldsymbol{E}}^\pi(\eta)\right)}{d\eta} = 0 \ , \ \eta \in [0,1]\right\} \tag{41}$$

5. *Compute energy value:*

$$G_{\alpha\beta} = \widetilde{\Pi}\left(\lambda^\pi, \widetilde{\boldsymbol{E}}^\pi(\lambda^\pi)\right) \tag{42}$$

6. *RETURN*

Note that steps 4 and 5 may be combined into an equivalent statement

$$G_{\alpha\beta} = \max_{\eta \in [0,1]} \left\{\widetilde{\Pi}\left(\eta, \widetilde{\boldsymbol{E}}^\pi(\eta)\right)\right\} \tag{43}$$

which proves convenient when determining λ^π. After the discrete form of the equations are derived in the following section, the numerical solution of Eq.(43) can be achieved by any of a number of bounded iteration schemes.

11

4. DISCRETE FORM: IMPLEMENTATION

In this section we briefly consider some aspects of the discrete form of the constitutive model which are needed in order to solve general boundary value problems. It is assumed that the model is to be implemented within a traditional strain driven finite element code, so we will consider implementation of the constitutive model as an independent entity within an unspecified array of integration points. As such, the constitution will have available to it the current strain and temperature values $(\boldsymbol{E}_{n+1}, \theta_{n+1})$ at time t_{n+1}, as well as the previous history variables $\boldsymbol{\xi}_n$. Of interest is the computation of the updated stress value $\boldsymbol{S}_{n+1}$, the updated volume fractions $\boldsymbol{\xi}_{n+1}$, and the algorithmic tangent $\mathbb{C}^{alg}$. The notation adopted in this section denotes quantities evaluated at times t_n and t_{n+1} (where $t_{n+1} = t_n + \Delta t$, $\Delta t > 0$) by the subscripts n and $n+1$ respectively.

In advancing the discrete form of the constitution from time t_n to time t_{n+1}, we begin by writing the effective modulus, stress and rate matrix at time t_{n+1}:

$$\mathbb{C}_{n+1} = \sum_\alpha \xi_{n+1}^\alpha \mathbb{C}^\alpha \tag{44}$$

$$\boldsymbol{S}_{n+1} = \sum_\alpha \xi_{n+1}^\alpha \mathbb{C}^\alpha : [\boldsymbol{E}_{n+1} - \boldsymbol{E}^{\alpha_t} - \Delta\theta_{n+1}\boldsymbol{E}^{\alpha_\theta}] \tag{45}$$

$$\boldsymbol{Q}_{n+1} = \widehat{\boldsymbol{Q}}(\boldsymbol{S}_{n+1}, \theta_{n+1}) \tag{46}$$

where $\Delta\theta_{n+1} = \theta_{n+1} - \theta_o$ is the relative temperature change at time $n+1$. Note that $\mathbb{C}^\alpha$, $\boldsymbol{E}^{\alpha_t}$, and $\boldsymbol{E}^{\alpha_\theta}$ are material constants. The last line, Eq.(46), gives the functional dependency of the discrete generator $\boldsymbol{Q}_{n+1}$ as needed for the integration method described next.

The choice of a discrete form for Eq.(32) is critical to the computational expense of the implementation, and as such has been the subject of prior investigation. With regard to the solution of the nonlinear discrete constitutive equations, the problem is sensitive to variations which violate mass conservation. For this reason, Govindjee & Hall (1999b) outlined the use of a simple integration rule in combination with explicit enforcement of the physical principal of mass balance. This allows one to use a "Backward Euler" rule

$$\begin{aligned}\boldsymbol{\xi}_{n+1} &= \boldsymbol{\xi}_n + \Delta t \boldsymbol{Q}_{n+1}\boldsymbol{\xi}_{n+1} \\ &= (\mathbf{1} - \Delta t\boldsymbol{Q}_{n+1})^{-1}\boldsymbol{\xi}_n = \boldsymbol{H}_{n+1}\boldsymbol{\xi}_n\end{aligned} \tag{47}$$

along with an explicit orthogonal projection to the space of volume fractions satisfying Eq.'s(16,21). This projection is performed during the constitutive iteration defined by the residual function

$$\boldsymbol{f}(\boldsymbol{\xi}_{n+1}) = \boldsymbol{\xi}_{n+1} - \boldsymbol{H}_{n+1}\boldsymbol{\xi}_n. \tag{48}$$

Due to the convexity of the constraint space, the projection has the attractive feature of always reducing the error in the integration. Furthermore, the composite solution strategy was found in one dimension to be accurate and efficient for our particular application. A summary of the solution strategy, details of which are given in Govindjee & Hall (1999a, 1999b), is shown in Algorithm 2.

ALGORITHM 2. Constitutive Iteration

1. *Input at time t_{n+1}:*

$$\{\boldsymbol{E}_{n+1} \quad , \quad \theta_{n+1} \quad , \quad \boldsymbol{\xi}_n\} \tag{49}$$

2. *Initialize values:*

$$\boldsymbol{S}^{(k)} = \widehat{\boldsymbol{S}}\left(\boldsymbol{E}_{n+1}, \theta_{n+1}, \boldsymbol{\xi}_n\right) \tag{50}$$

$$\boldsymbol{\xi}^{(k)} = \boldsymbol{\xi}_n \tag{51}$$

3. *Compute the residual function:*

$$\mathbf{f}^{(k)} = \boldsymbol{\xi}^{(k)} - \boldsymbol{H}^{(k)}\boldsymbol{\xi}_n \tag{52}$$

4. *IF* $\|\mathbf{f}\|_\infty <$ *TOL THEN*

$$\boldsymbol{\xi}_{n+1} = \boldsymbol{\xi}^{(k)} \tag{53}$$

$$\boldsymbol{S}_{n+1} = \boldsymbol{S}^{(k)} \tag{54}$$

$$\mathbb{C}^{alg}_{n+1} = \frac{\partial \boldsymbol{S}_{n+1}}{\partial \boldsymbol{E}_{n+1}} \tag{55}$$

$$\text{RETURN} \Rightarrow \text{END} \tag{56}$$

5. *ELSE*

$$\boldsymbol{\xi}^{(k+1)} = \boldsymbol{\xi}^{(k)} - \kappa \left[\nabla_\xi \mathbf{f}^{(k)}\right]^{-1} \mathbf{f}^{(k)} \tag{57}$$

$$\boldsymbol{S}^{(k+1)} = \widehat{\boldsymbol{S}}\left(\boldsymbol{E}_{n+1}, \theta_{n+1}, \boldsymbol{\xi}^{(k+1)}\right) \tag{58}$$

$$k = k+1 \tag{59}$$

6. *GOTO STEP 3*

As clarification, it is noted that during the constitutive iteration, the aforementioned projection is only performed when the volume fractions leave the constraint space. Secondly, $\mathbb{C}^{alg}_{n+1}$ denotes the algorithmic tangent (Simo & Taylor 1986) arrived at by the linearization $\partial \boldsymbol{S}_{n+1}/\partial \boldsymbol{E}_{n+1}$ of the discrete form of the continuum equations. The value of this consistent tangent, which is an essential component of the implementation in a finite element setting, is given by the expression

$$\mathbb{C}^{alg}_{qrkl} = \left[\mathbb{I}_{ijqr} - \sum_\alpha \sum_\beta S^\alpha_{ij}\frac{\partial H_{\alpha\beta}}{\partial S_{qr}}\tilde{\xi}^\beta\right]^{-1} \mathbb{C}_{ijkl} \tag{60}$$

where summation over roman indices is implied. The shorthand notation $\tilde{\boldsymbol{\xi}}$ was adopted for $\boldsymbol{\xi}_n$ to avoid confusion with subscripts; likewise time subscripts have been dropped in the understanding that unless noted otherwise, all quantities are evaluated at time t_{n+1}. The symbol $\mathbb{I}$ is the rank four identity tensor, and the remaining terms of Eq.(60) are defined as

$$S^\alpha_{ij} = \mathbb{C}^\alpha_{ijab}(E_{ab} - E^{\alpha_t}_{ab} - \Delta\theta E^{\alpha_\theta}_{ab}) \tag{61}$$

$$\mathbb{C}_{ijkl} = \sum_\beta \xi^\beta \mathbb{C}^\beta_{ijkl} \tag{62}$$

$$\frac{\partial H_{\alpha\beta}}{\partial S_{qr}} = \sum_\gamma \sum_\delta (\Delta t) H_{\alpha\delta}\frac{\partial Q_{\delta\gamma}}{\partial S_{qr}}H_{\gamma\beta} \tag{63}$$

13

To give an indication how an element of $\frac{\partial Q_{\delta\gamma}}{\partial S_{qr}}$ in Eq.(63) is computed, consider a single term $P_{\alpha\beta}$ from the matrix $\boldsymbol{Q}$. Using Eq.'s(33,34) it is found that

$$\frac{\partial P_{\alpha\beta}}{\partial S_{qr}} = \frac{-\Delta v P_{\alpha\beta}}{k\theta}\left(\frac{\partial G_{\alpha\beta}}{\partial S_{qr}} - \frac{\partial G_{\alpha}}{\partial S_{qr}}\right). \tag{64}$$

Although the second term $\frac{\partial G(\boldsymbol{S},\theta,\xi^\alpha=1)}{\partial \boldsymbol{S}} = -(\mathbb{C}^\alpha)^{-1}:\boldsymbol{S} - \boldsymbol{E}^{\alpha t} - \boldsymbol{E}^{\alpha\theta}$ may be computed simply from Eq.(30), the first term $\frac{\partial G_{\alpha\beta}}{\partial S_{qr}}$ warrants further clarification. Starting from Eq.(35) the linearization of the lagrangian $\widetilde{\Pi}$ may be written as the sum of the four terms

$$\frac{d\widetilde{\Pi}}{d\boldsymbol{S}} = \frac{\partial\widetilde{\Pi}}{\partial\boldsymbol{S}} + \frac{\partial\widetilde{\Pi}}{\partial\theta}\frac{\partial\theta}{\partial\boldsymbol{S}} + \frac{\partial\widetilde{\Pi}}{\partial\boldsymbol{E}}:\frac{\partial\boldsymbol{E}}{\partial\boldsymbol{S}} + \frac{\partial\widetilde{\Pi}}{\partial\lambda}\frac{\partial\lambda}{\partial\boldsymbol{S}}. \tag{65}$$

This expression may be simplified by considering that the numerical evaluation of the tangent only occurs at the solution point given by $G_{\alpha\beta} = \widetilde{\Pi}(\boldsymbol{E}^\pi,\lambda^\pi)$ as previously defined. Looking at Eq.(65), it is seen that the first components of the third and fourth terms are the first and second critical equations of the lagrangian respectively (Eq.'s 36,37). As such, they do not contribute to the barrier height tangent with respect the stress when evaluated at the critical point of the lagrangian. Further noting that the current implementation treats the temperature as an assigned field eliminates the second term of Eq.(65) leaving only the result

$$\frac{dG_{\alpha\beta}}{d\boldsymbol{S}} = \left.\frac{\partial\widehat{\Pi}}{\partial\boldsymbol{S}}\right|_{(\lambda^\pi,\boldsymbol{E}^\pi)} = -\boldsymbol{E}^\pi \tag{66}$$

for the particular combination of variants α and β. As a final note, it should be stated that in the assembly of contributions from each term $P_{\alpha\beta}$ to the algorithmic tangent described by Eq.'s(60-63), care must be taken to properly account for the mapping between tensors and matrices. Doing so ensures the desirable global convergence properties observed in the examples given in the next section.

5. NUMERICAL SIMULATIONS

The examples provided in this section are intended to demonstrate the behavior of the model under various thermomechanical loading patterns. After a brief discussion of the requisite material parameters, the first group of examples concern the simulation of a material with cubic $\leftrightarrow$ tetragonal symmetry in the phase change. In particular, the simulations touch upon aspects of the resulting recoverable strain set, the observance of both pseudoelastic and martensitic transformations, and the prediction of polycrystalline behavior.

The second group of examples are with regard to a material which may undergo cubic $\leftrightarrow$ orthorhombic transformations. After beginning with a baseline example on the volume fraction evolution in the pseudoelastic region, the next example simulates nonhomogeneuos combined shear-axial loading of a shape memory plate. The final example simulates the behavior of a tube undergoing torsion with various boundary conditions. In particular, axially unrestricted torsion is compared with torsion-tension and torsion-compression behaviors.

Material Parameters

Regardless of the particular material under consideration, the constitution requires the specification of the following material parameters: austenite and martensite elasticity tensors ($\mathbb{C}^{\alpha=1}$, $\mathbb{C}^{\alpha \neq 1}$), austenite and martensite thermal expansion tensors ($\boldsymbol{E}^{\alpha_\theta=1_\theta}$, $\boldsymbol{E}^{\alpha_\theta \neq 1_\theta}$), the martensitic Bain strains ($\boldsymbol{E}^{\alpha_t}$), the attempt frequency (ω), the transformation volume (Δv), the heat capacity (c), the latent heat (λ_t), and the reference density (ρ_o). Additionally, the relative orientation of the variants must be known in order to "properly align" the martensitic properties. For example, Nenno & Saburi (1981) provide the orientation of the lattice vectors of each of the martensitic correspondence variants with regard to a basis aligned with the parent cubic austenite. These authors also provide the Bain strain broken down into a shape change $\boldsymbol{B}$ and a shearing motion $\boldsymbol{P}$ in a basis oriented along a given basal plane of the martensite. To obtain the homogenous transformation deformation with regard to a basis oriented along the austenite lattice vectors one must compute

$$\boldsymbol{F}^\alpha = (\boldsymbol{R}^\alpha)\boldsymbol{P}\boldsymbol{B}(\boldsymbol{R}^\alpha)^T \tag{67}$$

for each of the variants α. While this locates the martensite relative to the austenite, it is still necessary to orient the parent austenite basis with regard to the chosen reference basis for the problem. In the current implementation, a single set of martensite material properties are initially constructed with respect to the user input orientation of the cubic parent axes. By then looping over the number of variants, each of these are rotated into their respective orientations using the $\boldsymbol{R}^\alpha$ relations. The geometric properties for the problems considered herein are summarized in Appendix A.

Tables 1 and 2 list the chosen material parameters for the cubic $\leftrightarrow$ tetragonal and cubic $\leftrightarrow$ orthorhombic simulations respectively; the input required for orientation is given in Appendix A. The data entries in the tables were culled from a wide variety of sources (Robertson 1990, Nenno & Saburi 1981, Russell 1998, Yasunaga, Funatsu, Kojima, Otsuka & Suzuki 1983, Hosford 1993, Suezawa & Sumino 1976), and as such do not accurately represent a specific material but rather a generic material of the given class. For this reason, as well as the fact that we have not included the effects of plasticity, the examples in the following sections are intended to primarily demonstrate the qualitative strength of the model. We begin by considering a material with three variants of martensite.

Cubic $\leftrightarrow$ Tetragonal

Example 1: Applied strain path.

As a first example we consider the response of the constitution to an imposed strain path in the direction of the second martensitic bain strain ($\alpha_t = 3_t$)

$$\boldsymbol{E}(t) = \kappa(t)\boldsymbol{E}^{3_t} \tag{68}$$

where $\kappa(t)$ is a sawtooth load which varies between plus and minus one in magnitude. The strain rate is set at $1.d-4$ per second as computed from the norm of the Bain strain, while the temperature is fixed at 363 K for the duration of the run. The initial values of the volume fractions were chosen, consistent with the initial load and temperature, as purely austenite.

Table 1: APPROXIMATE PROPERTIES FOR A CUBIC-TETRAGONAL MATERIAL

Reference density	ρ	$= 6448.1$	kg/m^3
Austenite Properties	$\mathbb{C}_{1111} = \mathbb{C}_{2222} = \mathbb{C}_{3333}$	$= 141.0 \times 10^9$	Pa
(austenite basis)	$\mathbb{C}_{1122} = \mathbb{C}_{2233} = \mathbb{C}_{1133}$	$= 125.0 \times 10^9$	Pa
	$\mathbb{C}_{1212} = \mathbb{C}_{2323} = \mathbb{C}_{1313}$	$= 97.0 \times 10^9$	Pa
	$E_{11}^{\theta} = E_{22}^{\theta} = E_{33}^{\theta}$	$= 6.5 \times 10^{-6}$	1/K
Martensite Properties	$\mathbb{C}_{1111} = \mathbb{C}_{2222}$	$= 197.0 \times 10^9$	Pa
(martensite basis)	$\mathbb{C}_{3333}$	$= 141.0 \times 10^9$	Pa
	$\mathbb{C}_{1122}$	$= 45.5 \times 10^9$	Pa
	$\mathbb{C}_{2233} = \mathbb{C}_{1133}$	$= 119.5 \times 10^9$	Pa
	$\mathbb{C}_{1212}$	$= 19.7 \times 10^9$	Pa
	$\mathbb{C}_{2323} = \mathbb{C}_{1313}$	$= 58.8 \times 10^9$	Pa
	$E_{11}^{\theta} = E_{22}^{\theta}$	$= 6.0 \times 10^{-6}$	1/K
	E_{33}^{θ}	$= 6.5 \times 10^{-6}$	1/K
Latent heat	λ_t	$= 14.5 \times 10^3$	J/kg
Heat capacity	c	$= 4.0 \times 10^2$	J/(kg K)
Attempt frequency	ω	$= 12 \times 10^3$	1/s
Transformation volume	Δv	$= 1.612 \times 10^{-27}$	m^3
Martensitic Bain strain	$E_{11} = E_{22}$	$= -0.0608$	
(martensite basis)	E_{33}	$= 0.1302$	

By the response indicated in Figure 2, it is seen that as expected, the model predicts the formation of the second variant as κ grows above zero. In contrast, the negative strain path ($\kappa(t) < 0$) forms an equal mixture of the first and third variants qualitatively predicting a twin formation. In both cases, the unloading path sees a return to austenite as the load is removed.
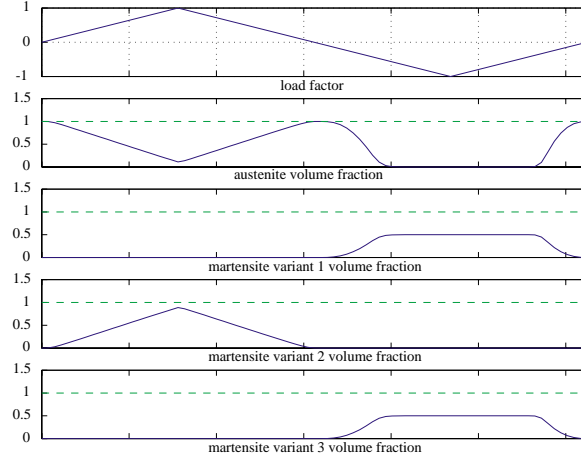

Figure 2. Pseudoelastic variation of the volume fractions for a tetragonal shape memory alloy under mechanical cycling. The first plot gives the loading pattern function $\kappa(t)$ from Eq.(68). The remaining plots show the evolution of the volume fractions under the load for austenite and each of the martensitic variants. In each case the dashed line is the sum of the volume fractions.

Table 2: Approximate Properties for a Cubic-Orthorhombic Material

Reference density	ρ	$= 6448.1$	kg/m^3
Austenite Properties	$\mathbb{C}_{1111} = \mathbb{C}_{2222} = \mathbb{C}_{3333}$	$= 141.0 \times 10^9$	Pa
(austenite basis)	$\mathbb{C}_{1122} = \mathbb{C}_{2233} = \mathbb{C}_{1133}$	$= 125.0 \times 10^9$	Pa
	$\mathbb{C}_{1212} = \mathbb{C}_{2323} = \mathbb{C}_{1313}$	$= 97.0 \times 10^9$	Pa
	$E_{11}^\theta = E_{22}^\theta = E_{33}^\theta$	$= 6.5 \times 10^{-6}$	1/K
Martensite Properties	$\mathbb{C}_{1111}$	$= 189.0 \times 10^9$	Pa
(martensite basis)	$\mathbb{C}_{2222}$	$= 141.0 \times 10^9$	Pa
	$\mathbb{C}_{3333}$	$= 205.0 \times 10^9$	Pa
	$\mathbb{C}_{1122}$	$= 124.0 \times 10^9$	Pa
	$\mathbb{C}_{2233}$	$= 119.5 \times 10^9$	Pa
	$\mathbb{C}_{1133}$	$= 45.5 \times 10^9$	Pa
	$\mathbb{C}_{1212}$	$= 62.6 \times 10^9$	Pa
	$\mathbb{C}_{2323}$	$= 54.9 \times 10^9$	Pa
	$\mathbb{C}_{1313}$	$= 19.7 \times 10^9$	Pa
	E_{11}^θ	$= 6.5 \times 10^{-6}$	1/K
	E_{22}^θ	$= 4.5 \times 10^{-6}$	1/K
	E_{33}^θ	$= 6.0 \times 10^{-6}$	1/K
Latent heat	λ_t	$= 10.0 \times 10^3$	J/kg
Heat capacity	c	$= 4.0 \times 10^2$	J/(kg K)
Attempt frequency	ω	$= 12.0 \times 10^3$	1/s
Transformation volume	Δv	$= 2.512 \times 10^{-27}$	m^3
Martensitic Bain strain	E_{11}	$= 0.0620$	
(martensite basis)	E_{22}	$= -0.0820$	
	E_{33}	$= 0.0230$	

Example 2: Pseudoelastic/Martensitic runs

Having considered the response of the constitution under an idealized strain path, we next consider a simple three dimensional boundary value problem. The problem consists of a 2 cm single crystal cube under an applied cyclic load along one of the major axes of the block. Displacement boundary conditions were chosen in a minimal fashion so that the block was free to expand/contract without restriction. The austenite lattice was set to be coincident with the orientation of the cube for each of the problems considered. The calculations were performed using the finite element program FEAP developed at the University of California at Berkeley (Taylor 1998).

The first run, the results of which are presented in Figure 3, shows the pseudoelastic response of the material to an applied sawtooth load pattern under a constant temperature of 363 K. Due to the homogenous nature of the stress pattern, runs with a single element and with a multiple element mesh produced identical results. Of interest in the response is the dramatic lack of symmetry observed between the tension and compression responses of the material; this is partially due to the explicit inclusion of elastic anisotropy in addition to the essential feature of non-symmetry in the recoverable strain set. Also it is noted that the recoverable strain varies dramatically depending upon the load path as would be expected in a material with a martensitic phase of such high symmetry.
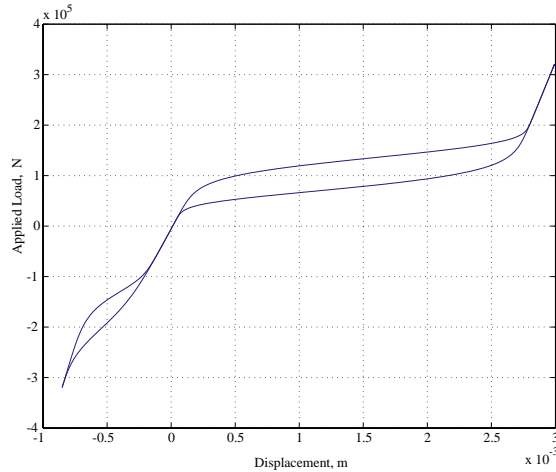
Figure 3. Pseudoelastic response under an applied cyclic load. The vertical axis indicates the response of the block in newtons, whereas the horizontal axis indicates displacement in the direction of the load measured in meters. Note the highly non-symmetric pseudoelastic response.
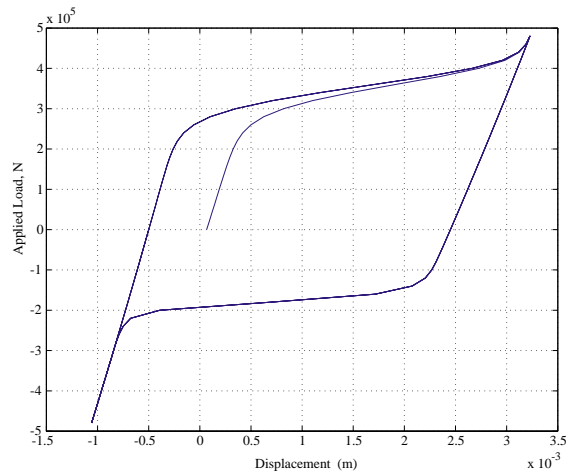

Figure 4. Martensitic transformation under an applied cyclic load. The vertical and horizontal axes measure reaction and displacement in the direction of the load in units of newtons and meters respectively. In contrast to Figure 3, this mechanical load cycle was applied at a significantly lower temperature and exhibits the type of hysteresis associated with martensitic transformations.

Figure 4 again shows the response of the block to an applied sawtooth load, only at a temperature of 243 K. In this case the initial martensitic fractions were set to $\boldsymbol{\xi} = \{0.0 \ , \ 0.34 \ , \ 0.34 \ , \ 0.32\}$. The resulting martensitic transformation again shows a lack of symmetry between tension and compression due to the formation of different volume fraction combinations at each extreme.

Example 3: Shape Memory Cycle.

The next numerical simulation illustrates a typical example of "shape memory" wherein an apparent residual deformation left from mechanical cycling is recovered through a subsequent thermal cycle. The material is assumed to begin in a state of equal martensitic volume fractions, under no load, and

at a temperature below what would be considered the martensitic finish temperature. The material is then subjected to several cycles of an applied load; the resulting martensitic transformations leaves the sample with a residual deformation. The temperature is then raised sufficiently to induce a phase transformation to austenite which has the effect of recovering the induced offset. The loading path is then closed by returning to the initial conditions by lowering the temperature back to the original value.

The numerical simulation of a process similar to that described above was applied to a 2 cm block where the initial equal martensitic volume fractions were aligned such that the parent (cubic) basis matched the primary axes of the block. Using minimal (unconstrained) boundary conditions for the problem, mechanical force loading was again applied along one of the major axes of the block with the resulting behavior shown in Figure 5. The three axes of this plot indicate the reaction of the block in newtons, the displacement of the block in the direction of the load, and the temperature value in the material. While the qualitative response of the model is quite reasonable, it is also significant that throughout both the mechanical and thermal cycles the global problem was observed to maintain a quadratic convergence rate; see Figure 13 for iteration residuals typical of the current implementation.
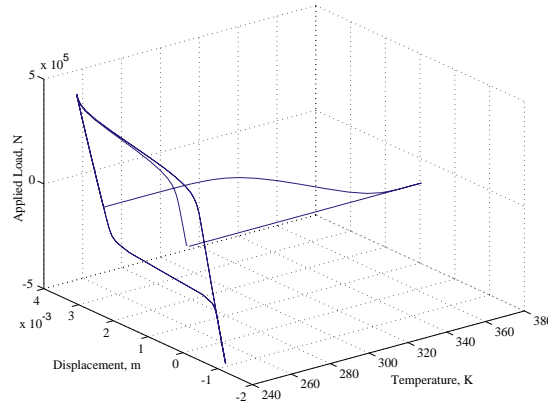

Figure 5. Shape memory cycle. After martensitic transformation leaves a residual deformation at zero load, a subsequent thermal cycle is seen to return the system to the initial configuration.

Example 4: High Symmetry Polycrystalline Simulation

The final simulations concerning a cubic $\leftrightarrow$ tetragonal material demonstrate the inhomogeneity induced in a polycrystalline material and its effect on the observance of shape memory phenomena. We begin by considering the application of the model to a problem constrained to planar strain. The chosen dimensions of the remaining two dimensional problem are 3 cm by 3 cm with boundary conditions such that an extension may be applied along the vertical axis while horizontal expansions/contractions remain unconstrained. Using this geometry two problems are considered; the first is that of a single crystal with the parent lattice along the reference axes; the second is of a polycrystal composed of sixteen randomly oriented grains (elements). In each case identical mechanical displacement loads are applied under a constant temperature of 343 K from an initial austenitic state.

19

From the resulting load deformation responses of the two problems, overlayed in Figure 6, it is apparent that the randomly oriented polycrystal exhibited essentially no transformation in comparison to the response of the single crystal. This result is consistent with theoretical calculations showing that alloys having a relatively high symmetry martensitic phase will not exhibit shape memory effects when in random or low texture polycrystalline form. As is reflected in the stress field of Figure 7, inhomogeneities induced by random grain orientations in polycrystalline materials hinder the cooperative motion required to achieve significant reorientation of the crystal structure. In particular, it has been proven that randomly oriented tetragonal polycrystals should not be expected to have any recoverable strain (Bhattacharya & Kohn 1996); our simulation reproduces this numerically.
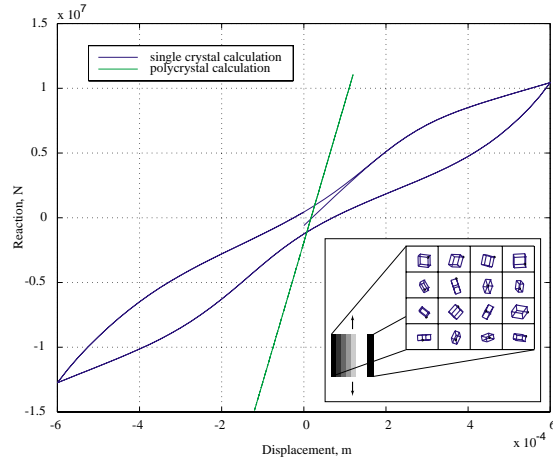
Figure 6. Comparison of single crystal (solid line) and multicrystal (dashed line) responses for a specimen in plane strain. The vertical axis indicates the reaction in newtons and the horizontal axis indicates the magnitude of the applied deformation in meters. The grains of the polycrystalline simulation were given a random orientation.

Cubic ↔ Orthorhombic

Example 5: Applied strain path.

This simulation serves as a baseline problem for the cubic ↔ orthorhombic class of materials described in Table 2 and used in subsequent examples. In a manner similar to that of Example 1, a strain is applied at a point along the path $\boldsymbol{E}(t) = \kappa(t)\boldsymbol{E}^{4t}$ where the load factor varies between ± 1 at a quasistatic strain rate. Since the orthorhombic crystal has six correspondence variants of martensite, Figure 8 tracks the evolution of the seven volume fractions with respect to the load. As the load approaches the Bain strain of the third martensitic variant ($\alpha_t = 4_t$), the material transforms to the appropriate variant. However, as the load factor reverses, the compressive structure is a combination of four variants of martensite of equal volume fraction indicating a complex twin structure. Since the temperature was held at 363 K for the simulation, intermediate (near zero) load factor values corresponded with a return to the initial condition of austenite.
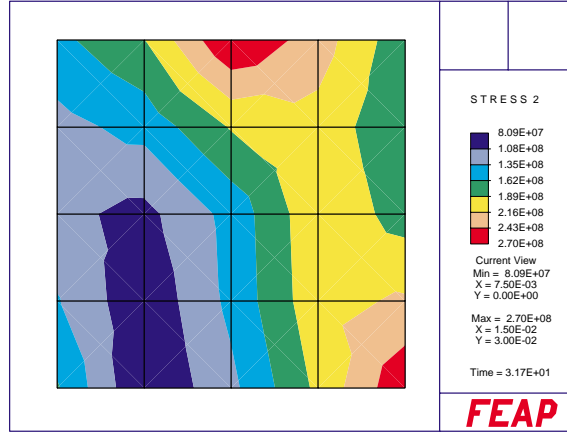
Figure 7. The inhomogeneity of stress reflects the random orientation of the grains in a polycrystal as represented by the materials in each element. The martensitic symmetry is too high to allow cooperative transformation between the crystals, hence the loss of shape memory effect seen in the previous figure.

Example 6: Shear panel.

The next example is a single crystal of a cubic ↔ orthorhombic material comprising a small panel measuring 6 cm wide (along X_2) by 12 cm tall (along X_1) and 2 cm thick (along X_3). This geometry is meshed in FEAP using eight node brick elements with boundary conditions that simulate fixed grips at the ends of the long (X_1) dimension of the panel so that it may be sheared in the $X_1 - X_2$ plane. The third dimension is supported on one plane, but otherwise is free to expand/contract perpendicular to X_3. The orientation of the parent lattice is set coincident with the reference axes, and the initial phase of the material is set to austenite.

A shearing deformation is then applied at $X_1 = 12$ in the X_2 direction while holding X_1 fixed. This results in a nonhomogeneous stress pattern as well as the development of reactions on the $X_1 = 0$ and $X_1 = 12$ planes. The reaction in the X_1 direction is henceforth referred to as the axial reaction, whereas the reaction in the X_2 direction is referred to as the shear reaction. These reactions are recorded as a fully reversed cycle of applied deformation is performed at a constant temperature of 363 K. Figure 9 plots both the net shear and axial responses against the lateral deflection. It is interesting to note that although the global response is essentially symmetric, the multiaxial and inhomogeneous nature of the stress field imparts any one point in the mesh with a nonsymmetric response with respect to the load cycle and the evolution of the volume fractions. This is reflected in Figure 10 which shows the average volume fraction history in an element centered at $\Delta X_2 = 1.5$cm , $\Delta X_1 = 1.2$cm from the center of the panel.

Example 7: Torsion tube

The final example is of a tube under several combinations of combined torsional and axial loading. The analysis was performed on a specimen with an inner radius of 2 mm and a wall thickness of 0.5 mm. The length of the analyzed section was set equal to the inner diameter of the tube, with fixed grip boundary conditions at either end. After meshing the geometry into eight node bricks as shown in Figure 11, combinations of purely torsional and axial deformations were applied at the ends at an approximately quasistatic strain rate. The individual runs are described below.
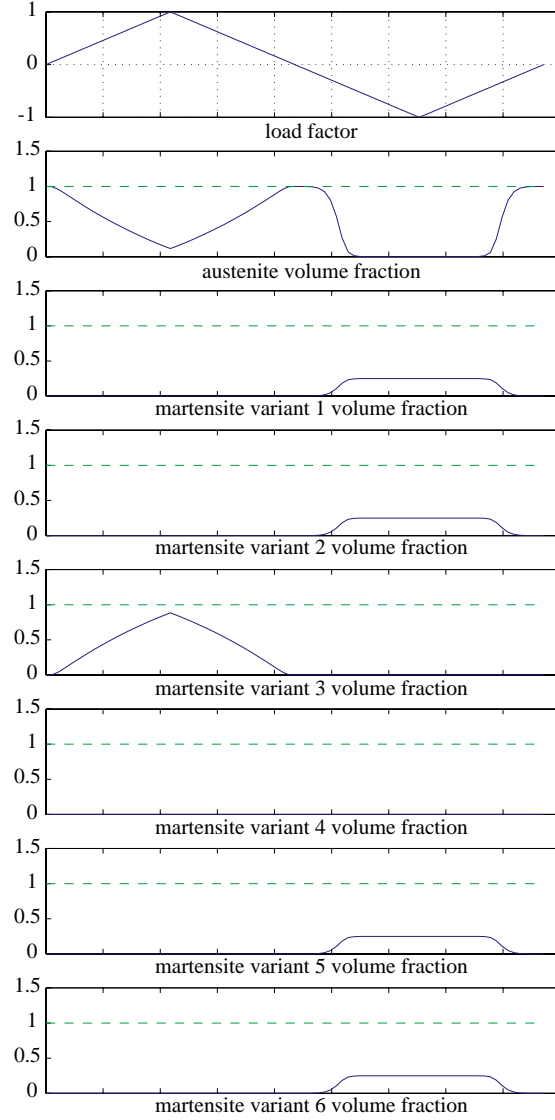
Figure 8. Pseudoelastic mechanical cycling of an orthorhombic shape memory alloy. The upper-most plot shows the load factor, while lower seven plots indicate the evolution of austenite and the six martensite variants relative to the applied deformation. On the negative load factor cycle equal volume fractions of martensite variants 1, 2, 5, and 6 are favored.

The first simulation applied the finite displacement torsional load while allowing for free axial deformation (zero force axial boundary conditions). The nonproportional loading was applied in increments of 0.5 degrees as measured from the centerline of the tube at the fixed grips. In the interest of comparing the response under various axial loads, the maximum angle imposed in all of the simulations was 5 degrees, even when this produced loads expected to induce permanent slip deformation in such materials. Similarly, the temperature and initial phase were set as 363 K and austenite for all of the runs; one of the major axes of the austenite was assumed to coincide with the major axis of the tube. The second simulation applied an axial extension in unison with the angular deformation, while the third simulation applied an axial compressive displacement in
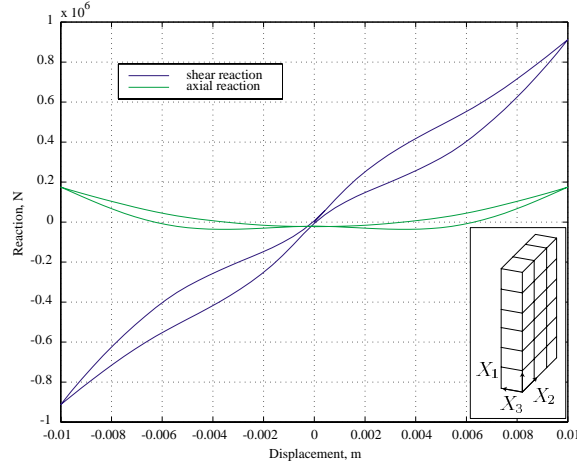
Figure 9. Pseudoelastic shear and axial responses of a cubic $\leftrightarrow$ orthorhombic panel to an applied shearing motion. The vertical axis indicates the net reaction in newtons, whereas the horizontal axis measures the lateral deflection in meters. The material and problem geometry are described in the text.
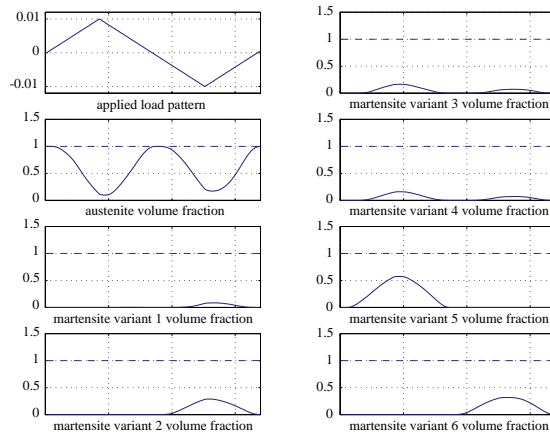

Figure 10. Volume fraction history at a point in the shear panel of Figure 9. The upper-left figure gives the applied displacement loading pattern for the global problem for comparison with the seven phase/variant plots. The dashed lines indicate the sum of the volume fractions.

combination with the torsion.

The load-reaction response of the three runs are presented in Figure 12 in the order just described from top to bottom. A comparison of the axially free torsion and torsion with axial extension reveals a lowering of the initial transformation load and slightly flatter plateau in the torque-angle response with the addition of tension. Conversely, the addition of compression has the opposite effect of increasing the apparent transformation load as seen in the third torque-angle plot. The response is qualitatively consistent with previous pseudoelastic experimental torsion-tension tests conducted on shape memory alloys of a different material class (Sittner, Hara & Tokuda 1995). Computationally, the global problem shows excellent convergence properties as indicated in Figure 13.
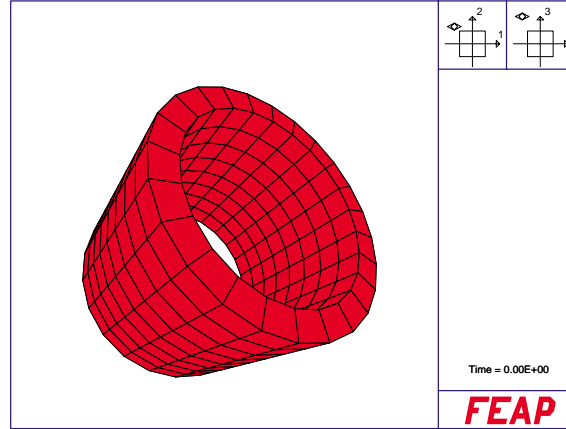
Figure 11. Torsional tube mesh from FEAP. Fixed grip boundary conditions were applied to the top and bottom of the tube for the axial driven problems; zero force boundary conditions were enforced for the axially free run.

6. DISCUSSION

The focus of the presented research is on the development of a computationally feasible framework for the modeling of shape memory alloys which is independent of dimension, provides robust performance in the solution of general boundary value problems, and is sufficiently general to incorporate the different material symmetry classes.

- In particular it is noted that choosing an energetic structure for the model allows us to side step complex issues associated with making difficult choices about transformation surface criteria that appear in SMA models more closely aligned with plasticity and generalized plasticity theory.

- The required barrier height computations have been worked out in detail and it has been shown how they may be computed for general multidimensional settings.

- The model is seen to be properly linearized for the purpose of solving implicit finite element problems in an efficient manner (i.e. with quadratic convergence when a Newton method is employed). The overall behavior of boundary value problems under a wide range of thermo-mechanical loadings has been observed to be highly robust.

- The model has been found to provide physically reasonable response for two classes of shape memory alloys despite the fact no attempt has been made to account for intricacies such as interfacial energy, intermediate plate twinning or plasticity. Complex behavior such as variant twin pairs and unsymmetric tension-compression behavior arise naturally from the proposed energetic structure. Further, the model is seen to reproduce important estimates on recoverable strains in high symmetry martensites and qualitatively reproduce prior multi-axial experiments on axial-torsion loadings.

Not withstanding the demonstrated power of the model structure, there remain important issues to address from both a modeling perspective and a computational perspective.

24

- The model at present does not incorporate interfacial energies or plate variants. To date it is not entirely clear what the structure of these terms should be. However it is noted that the model framework naturally allows for them to be included.

- The effects of plastic deformation need to be included if certain important industrial processes are to be simulated with the proposed model. Given the structure, a natural choice would be an activation energy based plasticity model.

- There is a large amount of anisotropic data that needs to be collected for the use of the model. To date such a complete set of data has not been reported on any given single material. Thus an effort needs to be made to collect such data. On the flip side an investigation needs to be made on the sensitivity of the model to such aspects as the elastic anisotropy; i.e. it is quite possible that utilizing isotropic moduli would provide reasonable predictions for an engineering purpose and at the same time simplify some of the computations.

These last three points are all the subject of an ongoing research and will be reported upon shortly.

ACKNOWLEDGMENTS

REFERENCES

Abeyaratne, R. & S.J. Kim. 1997. "Cyclic Effects in Shape-Memory Alloys: A One-Dimensional Continuum Model." *International Journal of Solids and Structures* 34:3273–3289.

Abeyaratne, R., S.J. Kim & J.K. Knowles. 1994. "A One-Dimensional Continuum Model for Shape-Memory Alloys." *International Journal of Solids and Structures* 31:2229–2249.

Achenbach, M. 1989. "A Model for an Alloy with Shape Memory." *International Journal of Plasticity* 5:371–395.

Achenbach, M. & I. Müller. 1985. "Simulation of Material Behavior of Alloys with Shape Memory." *Archives of Mechanics* 35:537–585.

Atkin, R.J. & R.E. Craine. 1976. "Continuum Theories of Mixtures: Basic Theory and Historical Development." *The Quarterly Journal of Mechanics and Applied Mathematics* 29:209–244.

Ball, J.M. & R.D. James. 1987. "Fine Phase Mixtures as Minimizers of Energy." *Archive for Rational Mechanics and Analysis* 100:13–52.

Ball, J.M. & R.D. James. 1992. "Proposed Experimental Tests of a Theory of Fine Microstructure and the Two Well Problem." *Philosophical Transactions of the Royal Society of London* 338:389–450.

Bhattacharya, K. 1993. "Comparison of the Geometrically Nonlinear and Linear Theories of Martensitic Transformation." *Continuum Mechanics and Thermodynamics* 5:205–242.

Bhattacharya, K. & R.V. Kohn. 1996. "Symmetry, Texture, and the Recoverable Strain of Shape Memory Alloys." *Acta Metallurgica* 44:529–542.

Bhattacharya, K. & Y.C. Shu. 1998. "The Influence of Texture on the Shape-Memory Effect in Polycrystals." *Acta Materialia* 46(15):5457–5473.

Boyd, J.G. & D.C. Lagoudas. 1996*a*. "A Thermodynamic Constitutive Model for the Shape Memory Materials. Part I. The monolithic shape memory alloy." *International Journal of Plasticity* 12:805–842.

Boyd, J.G. & D.C. Lagoudas. 1996*b*. "A Thermodynamic Constitutive Model for the Shape Memory Materials. Part II. The sma composite material." *International Journal of Plasticity* 12:843–873.

Carstensen, C. & P. Plecháč. 1997. "Numerical Solution to the Scalar Double-Well Problem allowing microstructure." *Mathematics and Computation* 66:997–1026.

Carstensen, C. & P. Plecháč. 1998. "Numerical Analysis of Compatible phase transitions in elastic solids." *Technical Report 98-16, Mathematisches Seminar, Christian-Albrechts-Universität zu Kiel* .

Govindjee, S. & G.J. Hall. 1999*a*. "A Computational Model for Shape Memory Alloys." *International Journal of Solids and Structures* 37:735–760.

Govindjee, S. & G.J. Hall. 1999*b*. "Computational Aspects of Solid-Solid Phase Transformation Modeling with a Gibbs Function." *SPIE, Smart Structures and Materials 1999: Mathematics and Control in Smart Structures* 3667:302–313.

Gurtin, M.E. 1983. "Two-Phase Deformations of Elastic Solids." *Archive for Rational Mechanics and Analysis* 84(1):1–29.

Hosford, W.F. 1993. *The Mechanics of Crystals and Textured Polycrystals.* Oxford University Press.

Huang, M. & L.C. Brinson. 1998. "A Multivariate Model for Single Crystal Shape Memory Alloy Behavior." *Journal of the Mechanics and Physics of Solids* 46(8):1379–1409.

Kohn, R.V. 1991. "The relaxation of a double well energy." *Continuum Mechanics and Thermodynamics* 3:193–236.

Lubliner, J. & F. Auricchio. 1996. "Generalized Plasticity and Shape Memory Alloys." *International Journal of Solids and Structures* 33:991–1003.

Milke, A., M.S. Kuczma & F. Theil. 1998. "Stress- and Strain-Induced Phase Transformations in Engineering Materials." *Preprint Nr. A10, Universität Hannover, Institut für Angewandte Mathematik.*

Nenno, S. & T. Saburi. 1981. "The Shape Memory Effect and Related Phenomena." *Proceedings of an International Conference on Solid Solid Phase Transformations* pp. 1455–1479.

Robertson, I.M. 1990. "Elastic properties of shape memory alloy martensites." *Scripta Metallurgica et Materialia* 24(10):1947–1952.

Russell, S. 1998. NiTi Technical Pages. Technical report Shape Memory Applications, Inc.

Simo, J.C. & R.L. Taylor. 1986. "Consistent Tangent Operators for Rate Independent Elastoplasticity." *Computational Methods in Applied Mechanics and Engineering* 48:101–118.

Sittner, P., Y. Hara & M. Tokuda. 1995. "Experimental Study on the Thermoelastic Martensitic Transformation in Shape Memory Alloy Polycrystal Induced by Combined External Forces." *Metallurgical and Materials Transactions A* 26(A):2923–2935.

Smyshlyaev, V.P. & J.R. Willis. 1999. "On the relaxation of a three-well energy." *Proceedings of the Royal Society of London A* 455:779–814.

Suezawa, M. & K. Sumino. 1976. "Behavior of Elastic Constants in Cu-Al-Ni Alloy in the Close Vicinity of Ms-Point." *Scripta Metallurgica* 10:789–792.

Taylor, R.L. 1998. "FEAP: A Finite Element Analysis Program." *http://www.ce.berkeley.edu/rlt/feap/.*

Truesdell, C. & R. Toupin. 1960. *The Classical Field Theories. HandBuch der Physik III/1.* Springer Verlag.

Truesdell, C. & W. Noll. 1965. *The Classical Field Theories. HandBuch der Physik III/3.* Springer Verlag.

Yasunaga, M., Y. Funatsu, S. Kojima, K. Otsuka & T. Suzuki. 1983. "Measurement of Elastic Constants." *Scripta Metallurgica* 17:1091–1094.

Zanzotto, G. 1996. "The Cauchy-Born Hypothesis, Nonlinear Elasticity and Mechanical Twinning in Crystals." *Acta Crystallographica* A52:839–849.

Table 4: ORIENTATION DATA

Cubic ↔ Tetragonal								
$Q^{\alpha=1}$			$Q^{\alpha=2}$			$Q^{\alpha=3}$		
0	0	1	$\frac{1}{\sqrt{2}}$	$\frac{1}{\sqrt{2}}$	0	$\frac{1}{\sqrt{2}}$	$-\frac{1}{\sqrt{2}}$	0
$\frac{1}{\sqrt{2}}$	$-\frac{1}{\sqrt{2}}$	0	0	0	1	$\frac{1}{\sqrt{2}}$	$\frac{1}{\sqrt{2}}$	0
$\frac{1}{\sqrt{2}}$	$\frac{1}{\sqrt{2}}$	0	$\frac{1}{\sqrt{2}}$	$-\frac{1}{\sqrt{2}}$	0	0	0	1

Cubic ↔ Orthorhombic								
$Q^{\alpha=1}$			$Q^{\alpha=2}$			$Q^{\alpha=3}$		
0	-1	0	0	-1	0	$\frac{1}{\sqrt{2}}$	0	$\frac{1}{\sqrt{2}}$
$\frac{1}{\sqrt{2}}$	0	$-\frac{1}{\sqrt{2}}$	$-\frac{1}{\sqrt{2}}$	0	$-\frac{1}{\sqrt{2}}$	0	-1	0
$\frac{1}{\sqrt{2}}$	0	$\frac{1}{\sqrt{2}}$	$\frac{1}{\sqrt{2}}$	0	$-\frac{1}{\sqrt{2}}$	$\frac{1}{\sqrt{2}}$	0	$-\frac{1}{\sqrt{2}}$
$Q^{\alpha=4}$			$Q^{\alpha=5}$			$Q^{\alpha=6}$		
$\frac{1}{\sqrt{2}}$	0	$-\frac{1}{\sqrt{2}}$	$\frac{1}{\sqrt{2}}$	0	$-\frac{1}{\sqrt{2}}$	$-\frac{1}{\sqrt{2}}$	0	$-\frac{1}{\sqrt{2}}$
0	-1	0	$\frac{1}{\sqrt{2}}$	0	$\frac{1}{\sqrt{2}}$	$\frac{1}{\sqrt{2}}$	0	$-\frac{1}{\sqrt{2}}$
$-\frac{1}{\sqrt{2}}$	0	$-\frac{1}{\sqrt{2}}$	0	-1	0	0	-1	0

APPENDIX A. MATERIAL ORIENTATION DATA

The relative orientation of each martensite variant lattice to the austenite lattice is required for the implementation of the model. In this section, the required alignment data used in the numerical simulations of Section 5 is presented. By limiting our attention to cubic ↔ tetragonal and cubic ↔ orthorhombic systems, we only need to be concerned with transformations between orthogonal basis vectors. For example, a change of coordinates between orthonormal bases $\boldsymbol{e}_i$ and $\boldsymbol{e}_{i'}$ is described by the tensor $\boldsymbol{Q}$ defined as

$$Q_{i'i} = \boldsymbol{e}_{i'} \cdot \boldsymbol{e}_i.$$

Transformations are then accomplished in the usual manner, e.g. $W_{i'j'} = Q_{i'i}Q_{j'j}W_{ij}$ for a rotation of the second order tensor $\boldsymbol{W}$.

The experimental data required to compute the transformation tensors ($\boldsymbol{Q}^\alpha$) is typically provided in the form of the basis vectors $\boldsymbol{e}_i$ locating the martensite basis with respect to the austenite basis. Table 4 summarizes one such set of data as reported by Nenno & Saburi (1981) for a cubic ↔ tetragonal material (Ni-Al) and cubic ↔ orthorhombic (Cu-Al-Ni) material respectively. Each entry gives a component of the tensor $Q_{pm} = \boldsymbol{e}_p \cdot \boldsymbol{e}_m$ where "m" indicates the normalized martensite basis vectors, and "p" indicates the austenite normalized basis vectors. In the present implementation we simply build the stiffness, Bain strain, and thermal coefficient tensors in the austenite basis input by the user. The $\boldsymbol{Q}$ mappings listed above then provide a means to rotate the tensors into the proper orientation with respect to the reference basis as described previously.
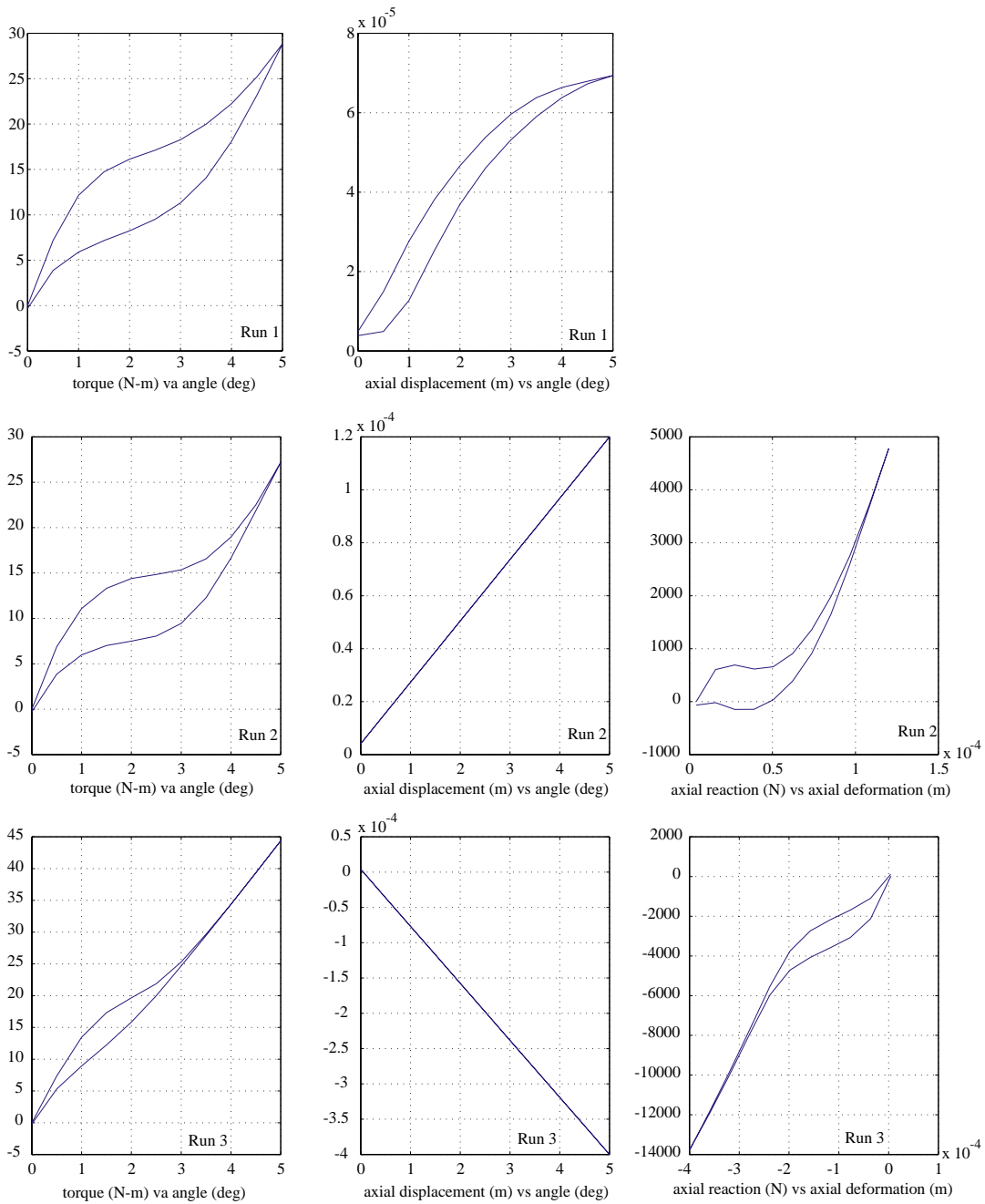
Figure 12. Combined torsion and axial loading of a cubic ↔ orthorhombic material tube. The left column of plots show the applied angle vs torque, the center column shows the applied axial displacement vs applied angle, and the right column plots give the axial response vs the axial deformation. The first row gives the results for free axial boundary conditions, the second gives the results for an applied extension, and the last row is for an applied compression. The units in all the plots are meters and newtons; the problem is described in the text and in Figure 11. The effect of axial loading on the pseudoelastic transformation, particularly compression in this example, is seen from the three simulations.
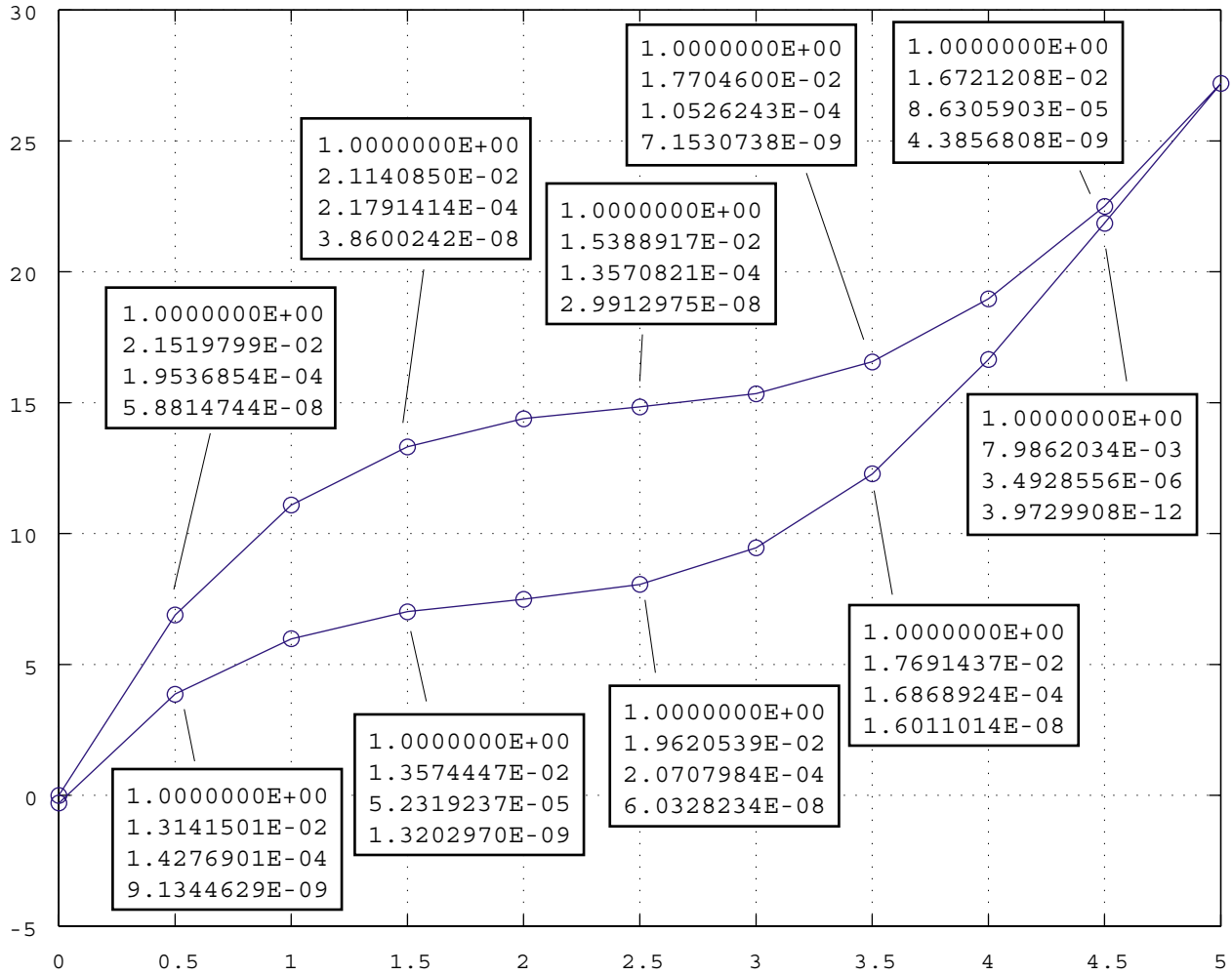


```
1.0000000E+00
1.7704600E-02
1.0526243E-04
7.1530738E-09
```

```
1.0000000E+00
1.6721208E-02
8.6305903E-05
4.3856808E-09
```

```
1.0000000E+00
2.1140850E-02
2.1791414E-04
3.8600242E-08
```

```
1.0000000E+00
1.5388917E-02
1.3570821E-04
2.9912975E-08
```

```
1.0000000E+00
2.1519799E-02
1.9536854E-04
5.8814744E-08
```

```
1.0000000E+00
7.9862034E-03
3.4928556E-06
3.9729908E-12
```

```
1.0000000E+00
1.3141501E-02
1.4276901E-04
9.1344629E-09
```

```
1.0000000E+00
1.3574447E-02
5.2319237E-05
1.3202970E-09
```

```
1.0000000E+00
1.9620539E-02
2.0707984E-04
6.0328234E-08
```

```
1.0000000E+00
1.7691437E-02
1.6868924E-04
1.6011014E-08
```

Figure 13. Convergence properties of the implementation. The convergence as measured in the residual norm (normalized to the first value) is given for every other step in the cycle. The problem shown is Run 1 from the torsion tube of Example 7; the convergence behavior is typical of all other simulations.